Head waves in ocean acoustic ambient noise: Measurements and modeling

Martin Siderius[a)]
Department of Electrical and Computer Engineering, Portland State University, Portland, Oregon 97201, USA

Jie Li and Peter Gerstoft
Noiselab, Scripps Institute of Oceanography, University of California, San Diego, 9500 Gilman Drive, La Jolla, California 92093, USA

(Received 27 July 2017; revised 21 January 2018; accepted 27 January 2018; published online 26 February 2018)

Seismic interferometry recovers the Green's function between two receivers by cross-correlating the field measured from sources that surround the receivers. In the seismic literature, it has been widely reported that this processing can produce artifacts in the Green's function estimate called "spurious multiples" or the "virtual refracted wave." The spurious multiples are attributed to the head wave and its multiples and travels in the seabed. The head wave phenomenon is shown to be observable from both controlled active sources and from ocean ambient noise and for both vertical and horizontal arrays. The processing used is a generalization of the passive fathometer to produce cross-beam correlations. This passive fathometer is equivalent to the seismic interferometry techniques for delay and sum beamforming but not for adaptive beamforming. Modeling and experimental data show the head wave is observed in ocean noise and can be used to estimate the seabed sound speed. © *2018 Acoustical Society of America*. https://doi.org/10.1121/1.5024332

[NPC] Pages: 1182–1193

I. INTRODUCTION

In seismic interferometry, signals measured on two or more receivers from the acoustic field produced by a set of surrounding sound sources are cross-correlated and integrated to produce an estimate of the Green's function, or impulse response, between these receivers. For active seismic interferometry,[1–3] the ideal configuration uses controlled point sources that surround a set of receivers. In some practical configurations, the controlled sources may not surround the receivers. Without controlled sources, the naturally occurring surface noise field (e.g., from wind and waves or ships) can be used but will not usually surround the receivers. This was demonstrated with ocean noise where it was identified that the sound sources along the line that connects the two receivers are the ones that primarily contribute to the Green's function estimate.[4–6] The Green's functions that result from this cross-correlation process can also produce what has been described as spurious multiples or virtual refraction and has been widely reported on using simulated data with active sound sources distributed near the sea-surface and measured on horizontal arrays.[7–9] The virtual refraction is a signal that arrives earlier in the estimated Green's function time series than is physically realizable. In this paper, this virtual refraction is shown to be due to head waves observed on both horizontal and vertical arrays with either active sources[10,11] or ocean ambient noise. A comparison is made between cross-correlation beamforming and seismic interferometry used to observe the head wave. The cross-correlation beamforming approach[12,13] has advantages that may prove valuable for seismic interferometry applications.

Wind and ocean waves create noise that can be used for remote sensing. These remote sensing methods are used for characterizing seabed properties,[14–17] array element localization,[18] Green's function recovery,[5,19] ocean tomography,[20] backscatter estimation,[12] or the passive fathometer.[15] In ocean acoustics, head waves have been observed in ocean noise by cross-correlating beams.[13] As head waves propagate in the seabed, they can be used for inferring seabed geo-acoustic properties.[10] Using time-domain cross-correlation beamforming, a passive method for measuring head waves and identifying seabed properties such as sound speed is developed.

The passive fathometer[15,21–25] method uses a vertical array of hydrophones to beamform surface generated noise. One beam is steered directly upward towards the surface noise and a second beam directly downward towards the seabed. The echo of the surface noise signal from the seabed is observed through time-domain cross-correlation of the upward and downward beams. This method can determine the travel time from the array to the seabed and the sub-bottom interfaces. This is, in effect, a fathometer and sub-bottom profiler but is passive, using only the naturally occurring surface noise.

In the initial development of the passive fathometer, anomalous peaks in noise field correlations were observed.[15] Wave fronts appeared in simulated data on a hydrophone array and as stated, "These wave fronts that occur at the critical angle suggest this process is detecting the head wave."[15] It was hypothesized that these anomalies could be due to the excitation of head waves,[26] however, there was little to support that claim other than the wavefronts propagating at the critical angle. More recently, this head wave hypothesis has been bolstered using modeling as well as measured data.[13]

The technique for observing these anomalous arrivals is a generalization of the passive fathometer processing and results

[a)]Electronic address: siderius@pdx.edu

are illustrated in Fig. 1 using ocean noise on a vertical array. The methodology used is described in Sec. IV and the experiment and data are described in Sec. V C. The cross-beam passive fathometer in Fig. 1 shows the cross-correlation between beams at different steered angles. The cross-beam correlation produces a time-lag that is converted to one-way travel distance by dividing by $2c$ (c is the ocean sound speed). The original passive fathometer returns occur by cross-correlating just the endfire beams ($\pm 90^\circ$), while the additional strong correlations occur by cross-correlating beams of $\approx \pm 10^\circ$. These peaks are due to the surface wave noise exciting head waves that reradiate into the water column at the seabed critical angle (10°). For the data in Fig. 1, the averaging time for the noise data is about 1 min. The beam widths vary depending on the steering direction with the endfire beams being widest so the spatial averaging depends on the steering direction. Although surface wind noise data are used here, other noise sources such as ship or aircraft noise[27] could be used. The spurious components visible at distances less than 5 m are due to the convolution of signals that do not propagate in the beam direction (details are given in Fig. 1 of Ref. 23).

These strong cross-correlation peaks in the noise field as shown in Fig. 1 are the subject of this paper and are investigated as they relate to the head wave. In Sec. II, the head wave is described and illustrated using a simulation of active sources received on a horizontal array. This is similar to the seismic interferometry work in Refs. 9 and 28. That work is extended here to include passive processing using surface (breaking wave) noise as the sound sources. In Sec. III, the method is expanded to application on vertical arrays for both active and passive configurations. Section IV describes the cross-beam processing which extracts the head waves from naturally occurring ambient noise. In Sec. V, four experimental data sets are examined to illustrate the processing in different locations using various array configurations and frequency bands. In some experimental data the head waves are relatively clear, however, in some cases not as much.

II. SEISMIC INTERFEROMETRY WITH HORIZONTAL ARRAYS

In seismic interferometry, the Green's function $G(\mathbf{r}_B, \mathbf{r}_A)$ can be extracted from the cross-correlation of the pressure field in two locations given by position vectors $\mathbf{r}_A$ and $\mathbf{r}_B$. For sources far from the receivers, the basic equation is[29]

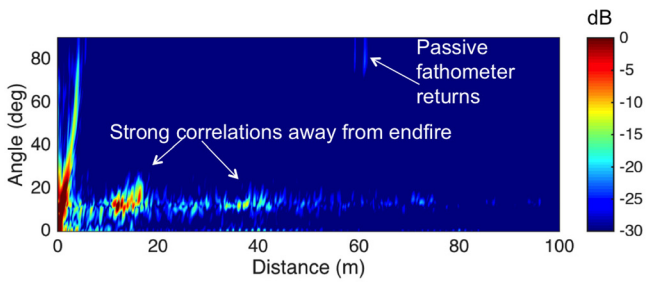

FIG. 1. (Color online) Beam cross-correlation of noise. The passive fathometer returns occur by cross-correlating endfire beams at $\pm 90^\circ$, while the anomalous correlations occur by cross-correlating beams of $\pm 10^\circ$. The x-axis is one-way travel distance.

$$G(\mathbf{r}_B, \mathbf{r}_A, \omega) + G^*(\mathbf{r}_B, \mathbf{r}_A, \omega) \propto \oint_{\partial S} G(\mathbf{r}_B, \mathbf{r}, \omega) G^*(\mathbf{r}_A, \mathbf{r}, \omega) d^2\mathbf{r}, \quad (1)$$

where ω is the angular frequency, $*$ indicates the conjugation operation, $G(\mathbf{r}_B, \mathbf{r}, \omega)$ and $G(\mathbf{r}_A, \mathbf{r}, \omega)$ represent the frequency domain Green's functions between a source on the closed boundary ∂S and a receiver positioned at $\mathbf{r}_B$ or $\mathbf{r}_A$.

The frequency domain Eq. (1) is transformed to the time domain,

$$G(\mathbf{r}_B, \mathbf{r}_A, \tau) + G(\mathbf{r}_B, \mathbf{r}_A, -\tau) \propto c(\mathbf{r}_B, \mathbf{r}_A, \tau), \quad (2)$$

where $G(\mathbf{r}_B, \mathbf{r}_A, \tau) + G(\mathbf{r}_B, \mathbf{r}_A, -\tau)$ corresponds to the superposition of causal and anti-causal Green's function, while the right-hand side $c(\mathbf{r}_B, \mathbf{r}_A, \tau)$ is the cross-correlation function between receivers at $\mathbf{r}_B$ and $\mathbf{r}_A$.

To estimate the exact Green's function, theory dictates that receivers are surrounded by a closed surface [indicated by the closed integral in Eq. (1)]. In that case, Eq. (2) indicates that the Green's function between $\mathbf{r}_B$ and $\mathbf{r}_A$ is recovered by measuring the field at these two points due to all the surrounding sources and then taking a cross-correlation. In practice, however, it is usual for the source aperture to be incomplete resulting in the appearance of what has been referred to as nonphysical arrivals, virtual refracted waves or spurious multiples.[7,30–33] These equivalent quantities are here referred to as the head wave.

To illustrate the head wave, simulations are used similar to those in Ref. 28, see Fig. 2. The full wavefield from each source (stars) to all receivers (triangles) was simulated using wavenumber integration. The full wavefield from the active sources (solid stars) and noise sources (hollow stars) was obtained from the ocean acoustic and seismic exploration synthesis (OASES) package.[34,35] The noise sources are

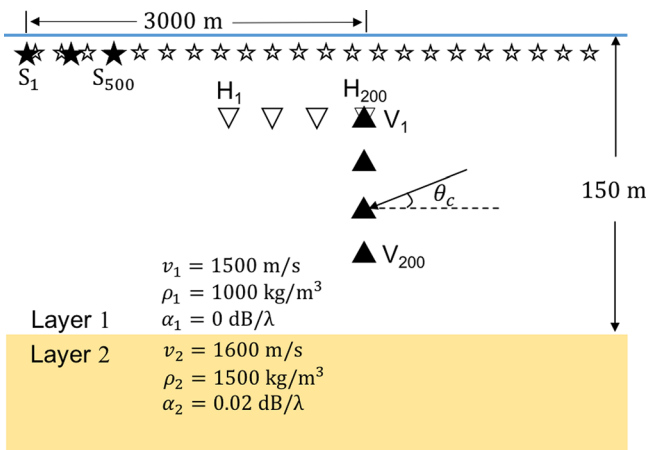

FIG. 2. (Color online) Model geometry showing ocean water column over a half-space and array geometry. The active source boundary (solid stars) containing 500 sources spaced every 4 m at 0.3 m depth. Noise sources (hollow stars) are located everywhere on the surface. H_1 to H_{200} form a horizontal array, 904 m from source S_{500}, sensor spacing 0.5 m, and array depth 20 m. V_1 to V_{200} forms a vertical array, 1004 m from source S_{500}, with the same aperture and spacing as the horizontal array, and the depth of V_1 is 20 m. θ_c is the critical grazing angle.

randomly phased and placed very near the surface, approximating the noise field generated by breaking waves.[36]

Two types of sources (controlled active and surface noise) and arrays (horizontal and vertical) form four acquisition geometries, which are, horizontal array active source (HA), horizontal array passive noise (HP), vertical array active source (VA), and vertical array passive noise (VP). For the passive case, the source is the noise generated at the sea-surface from wind and waves but potentially could be from other sources such as ship noise.

For near surface sources, propagating waves are assumed only downgoing from the source (i.e., the surface bounce path is not separable from the downward path), and both upgoing and downgoing at the receiver (see Fig. 3). The head wave travel time from source S to receiver r_j is the sum of travel times along the path in the water l_{water} and seabed l_{seabed}:

$$\begin{aligned} t_{sj} &= \frac{l_{\text{water}}}{v_1} + \frac{l_{\text{seabed}}}{v_2} = \frac{2mZ - z_s \pm z_j}{\sin\theta_c}\frac{1}{v_1} \\ &\quad + \left[x_j - x_s - (2mZ - z_s \pm z_j)\cot\theta_c\right]\frac{1}{v_2} \\ &= \frac{x_j - x_s}{v_2} + \frac{2mZ - z_s \pm z_j}{v_1 \sin\theta_c} - \frac{(2mZ - z_s \pm z_j)\cos^2\theta_c}{v_1 \sin\theta_c} \\ &= \frac{x_j - x_s}{v_2} + \frac{(2mZ - z_s \pm z_j)\sin\theta_c}{v_1}, \end{aligned} \tag{3}$$

where m is the number of bounce points from the bottom interface at depth Z that occur between the source and jth receiver, and using Snell's law for grazing angles, $v_2 = v_1/\cos\theta_c$, where v_1 and v_2 are sound speeds in the water and seabed. The signs in front of z_s and z_j in Eq. (3) correspond to the direction of the propagating waves. At the source, there is just a downgoing wave (i.e., $-z_s$) and at the receiver, there are both downgoing waves ($+z_j$) and upgoing ($-z_j$). From Eq. (3), the travel time difference[28] between receivers r_j and r_1 is [$\Delta_m = 0, \pm 1, \pm 2, \ldots$ is the difference in the ray paths between r_j and r_1 and is illustrated in Fig. 4(a)],

$$\delta t = t_{sj} - t_{s1} = \frac{x_j - x_1}{v_2} + \frac{(2\Delta_m Z \pm z_j \mp z_1)\sin\theta_c}{v_1}. \tag{4}$$

The results for observing the head wave for each of the four measurement configurations is described in the remainder of Sec. II and in Sec. III.

A. Horizontal array active (HA)

The head wave enters the seabed, travels within the seabed and re-radiates back into the water column. Head waves exist only for $v_2 > v_1$ and because it travels in the seabed at speed v_2, it is re-radiated back into the water column at exactly the critical grazing angle θ_c, as determined by Snell's law. For measurements in the water column, these head waves arrive ahead of other water borne arrivals. Therefore, the cross-correlation can appear to have precursor arrivals which led to this also being described as spurious multiples in the cross-correlation.[7]

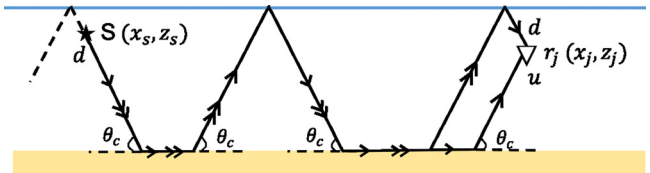

FIG. 3. (Color online) diagram showing head wave from source S to receiver r_j. Waves are downgoing (d) from the source and both upgoing (u) and downgoing (d) at the receiver.

The arrival of these head waves on horizontally separated receivers is diagrammed in Fig. 4. The head wave enters the seabed and then has various ray paths to the receivers. The receivers are not necessarily near the surface and therefore have both upgoing (u) and downgoing (d) receptions. There are then four combinations of possible head waves labeled: dd, du, ud, and uu as shown in Fig. 4.

For the horizontal array geometry, in Figs. 2 and 4, there is only a single array depth, z (dropping subscripts on z since $z_1 = z_j = z$). The travel time difference for the different paths from Eq. (4) is

$$\delta t = \frac{x_j - x_1}{v_2} + \frac{(2\Delta_m Z \pm z \mp z)\sin\theta_c}{v_1}. \tag{5}$$

For a given Δ_m, this produces three distinct travel times (corresponding to terms in parenthesis of $2\Delta_m Z + 2z$, $2\Delta_m Z, 2\Delta_m Z - 2z$) and is periodic in time with $2Z\sin\theta_c/v_1$ [or, for this configuration is $2 * 150 * \sin(20.4°)/1500 = 0.07$ s]. This interval is not related to array orientation or array spacing, since it is only a function of v_1, v_2 (via $\sin\theta_c$) and Z.

To observe the head wave, the processing involves measuring the acoustic field at H_1 through H_{200} due to the controlled, impulsive point sources near the surface (note, these sources are offset horizontally from the array). This is followed by cross-correlating over all sources N_S (500 here) and summing to create a virtual source at H_1,[3]

$$c_{j1}^{\text{A}}(\tau) = \sum_{k=1}^{N_S} h_k \mathcal{F}^{-1}(p_{jk}(\omega)p_{1k}^*(\omega)), \tag{6}$$

where h_k is a N_S- point spatial shading window (e.g., Hanning window), $\mathcal{F}^{-1}$ is the inverse Fourier transform operation, and $p_{jk}(\omega)$ is the sound pressure at receiver H_j from source S_k at frequency ω. The cross-correlation $c_{j1}^{\text{A}}(\tau)$ is an estimate of the time domain (τ) Green's function between the jth receiver and the receiver acting as the virtual source at receiver 1. For all the simulations shown the frequencies computed are every 0.25 Hz from 400 to 1000 Hz.

In Fig. 5(a), the envelope of $c_{j1}^{\text{A}}(\tau)$ shows the time domain Green's function with the left most receiver (H_1) acting as the virtual source. That is, the plot in Fig. 5(a) is similar to what would be observed if the left most receiver (H_1) were a source and the time-domain response is plotted for all j receivers $H_1 - H_{200}$ in rows of the plot. Note however, that because this active configuration uses only sources that are to one side and are offset horizontally it is not the same response as for a true source at H_1. For example, the arrivals are not symmetrical as that requires sources to be distributed

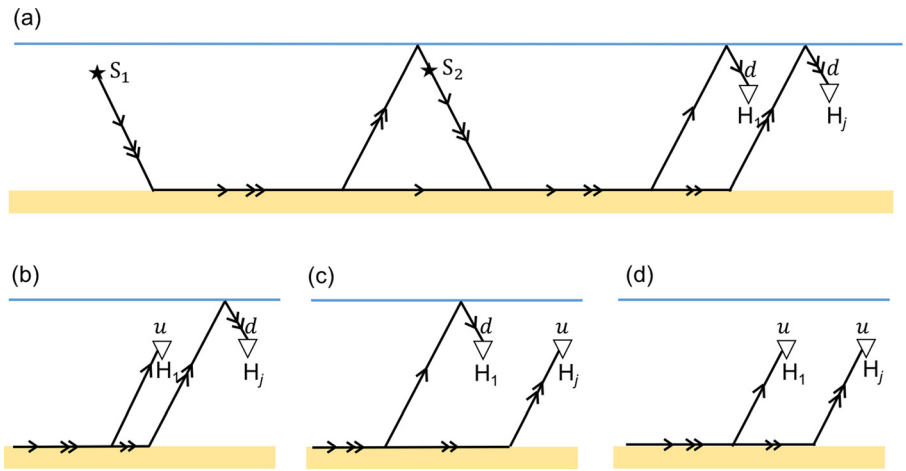

FIG. 4. (Color online) Ray diagram showing paths producing four head waves for two horizontal array elements, which are, *dd*, *du*, *ud*, and *uu* where *d* and *u* are short for downgoing and upgoing waves at the receiver. Panel (a) shows two source paths, a $\Delta_m = 0$ order head wave is shown from source S_2 and a $\Delta_m = 1$ order head wave from source S_1.

on both sides of the array. Figure 5(a), also shows the expected arrival times for various head wave correlations as discussed below (the possible combinations of paths are illustrated in Fig. 4). In Fig. 5(a), the dark areas indicate the arrival of wavefronts. The Δ_m along the top of Fig. 5(a), refers to difference in cross-correlation head wave order between H_j and H_1. Three groups of head waves with $\Delta_m = \pm 1$, and $\Delta_m = 0$, are observed in Fig. 5(a), while for $\Delta_m = 0$, the response is somewhat masked by the direct wave. Some of the higher order path differences (e.g., $\Delta_m = \pm 2$) are too weak to observe. The head wave propagates in the water column at the seabed critical angle. This can be seen from the slope of the head waves in Fig. 5(a) (e.g., the slope of the dashed and dash-dotted lines). To combine data, the rows of Fig. 5(a), are summed with time delays applied to each row in order to align the head wave response when summing. That is, $c_{j1}^{\mathrm{A}}(\tau)$ is summed over all receivers $j = 1, \ldots, N_R$ with time delay $(x_j - x_1)/v$ applied,

$$Y_{\mathrm{H}}(\tau, v) = \sum_{j=1}^{N_R} h_j c_{j1}^{\mathrm{A}}\left(\tau + \frac{x_j - x_1}{v}\right). \tag{7}$$

The envelope of $Y_{\mathrm{H}}(\tau, v)$ on a dB scale is shown in Fig. 5(b) and is similar to results in Ref. 28. To estimate the seabed sound speed v_2, the time delay $(x_j - x_1)/v$ is applied with hypothesized sound speed v. By summing the time-delayed sequences for a range of sound speeds v, a τ-v plot is produced with a maximum occurring at $v = v_2$, when the head waves sum constructively, as shown in Fig. 5(b). The isolated peaks at ± 0.07 s are from correlations $\Delta_m = \pm 1$, and they correspond to the correct sound speed v_2 (1600 m/s). Figure 5(c) shows the sound speed spectrum obtained by summing over τ the results in Fig. 5(b) for $0.04 < \tau < 0.2$ s. It peaks at the correct seabed sound speed v_2 (1600 m/s). The process described here is equivalent to a time-delay beamformer with delay times computed over values of seabed sound speed as opposed to the typical process of delaying over the steering angle.[37,38] This relationship to beamforming is described in Sec. IV.

To better show the summing process, Fig. 6 presents a waterfall plot of results in Fig. 5(a) after delaying according to v_2. All the traces are added coherently, producing the mean trace at the top, which corresponds $v = 1600$ m/s in Fig. 5(b).

B. Horizontal array passive (HP)

For passive ocean acoustic configurations the active sources are replaced with noise from the surface (HP case). In contrast to Eq. (6), the passive correlation c_{j1}^{P} is defined as

$$c_{j1}^{\mathrm{P}}(\tau) = \mathcal{F}^{-1}(p_j(\omega) p_1^*(\omega)), \tag{8}$$

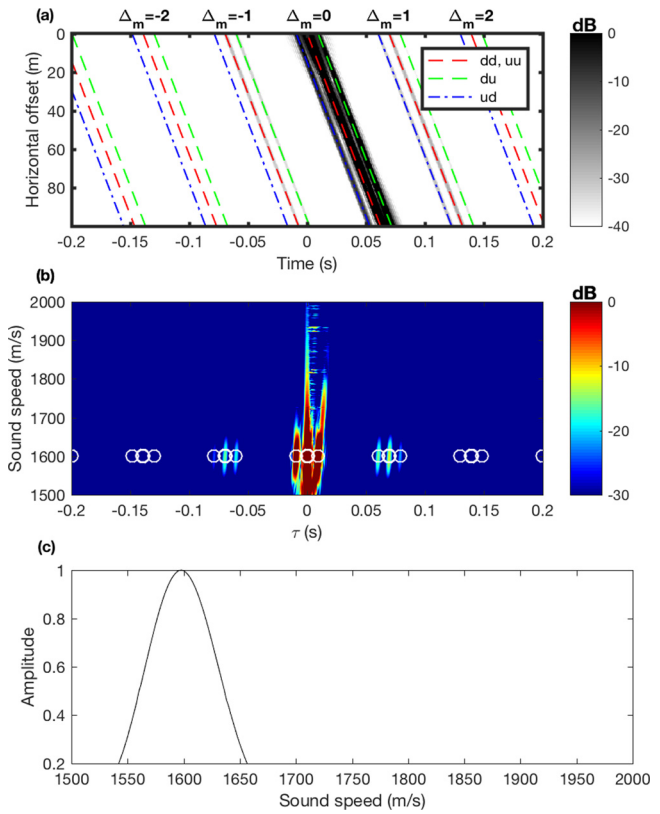

FIG. 5. (Color online) (a) Envelope of $c_{j1}^{\mathrm{A}}(\tau)$ in Eq. (6) for geometry HA in Fig. 2 with virtual source at H_1. The cross-correlation head wave arrival times Eq. (5) are shown as dashed and dash-dotted lines. In (b), the τ-v spectrum is shown by delay and sum of envelopes in (a) according to Eq. (7) with the expected locations of peaks (white circles). (c) Sound spectrum by summing results in (b) for $0.04 < \tau < 0.2$ s.

where $p_j(\omega)$, $j=1,\ldots,N_R$, is the sound pressure at receiver H_j due to ocean surface noise. For noise, the sources are already summed in $p_j(\omega)$ before the correlation and because the sources are not correlated with each other this also produces an estimate of the Green's function (see Ref. 3). The envelope of $c_{j1}^{P}(\tau)$, $j=1,\ldots,N_R$, is shown in Fig. 7(a). As with the previous case, there are four types of head wave arrivals (Fig. 4), but only three distinct arrival times. Comparing to the HA case (Fig. 5), the direct wave and head wave correlations $\Delta_m = \pm 1$ with positive slope, are visible in both HA and HP cases. However, the HP case has sources distributed on both sides of the array as opposed to only on the left side for the HA case. This leads to also having the negative slope head waves for HP. Surface reflected ("SR") waves and bottom reflected ("BR") waves are symmetrical in the time domain because sources are on both sides of the arrays and these were not visible in the HA case due to the placement of sources far from the array in that case (none directly overhead) which eliminated these arrivals. In the HP case, the sources more completely surround the array so the approximation to the true Green's function is better than for the HA case and therefore the SR and BR waves are much more visible in the HP case.

The τ-v spectrum is obtained by summing the positive slope head waves in Fig. 7(a) using Eq. (7) with c_{j1}^{P} instead of c_{j1}^{A}. The envelope of Y_H in dB is shown in Fig. 7(b). The peaks at ± 0.07 and ± 0.14 s correspond to the seabed sound speed 1600 m/s. The sound speed spectrum in Fig. 7(c) is obtained by summing results in Fig. 7(b) over the same interval as for Fig. 5(c).

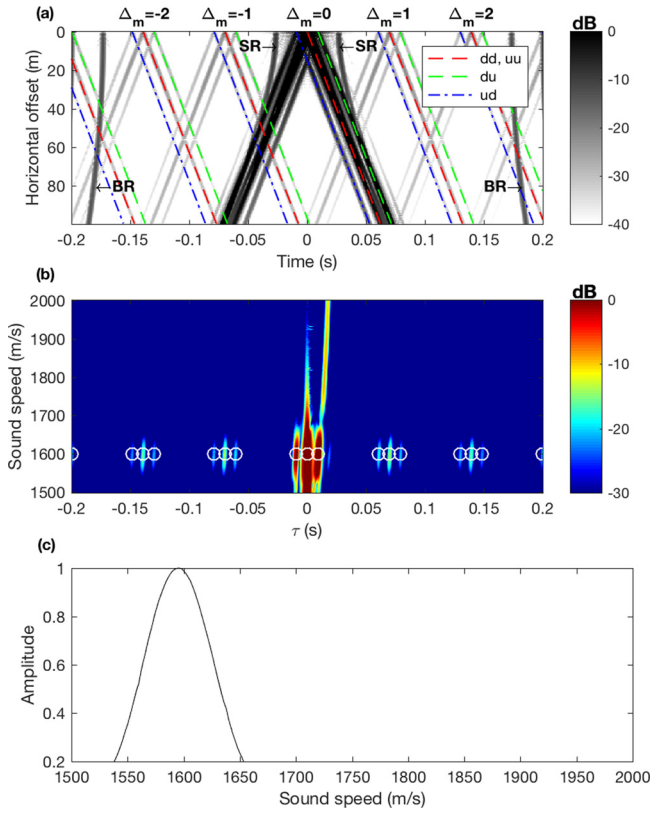

FIG. 7. (Color online) Similar as Fig. 5, but for geometry HP. In panel (a), the envelope of $c_{j1}^{P}(\tau)$ is shown and the surface-reflected wave (SR) and bottom-reflected wave (BR) are indicated. In (b), the τ-v spectrum is shown and in (c) the sum of results in panel (b).

III. SEISMIC INTERFEROMETRY WITH VERTICAL ARRAYS

A. Vertical array active (VA)

In this section, results are described for using a vertical array to observe the head wave and estimate seabed sound speed. The diagram for each head wave correlation is shown in Fig. 8. These four head wave arrivals will repeat according to the values of Δ_m and for each set the separation period is 0.07 s as for the horizontal array. For the vertical array configuration as shown in Fig. 2, the travel time difference equation becomes

$$\delta t = \frac{(2\Delta_m Z \pm z_j \mp z_1)\sin\theta_c}{v_1}. \tag{9}$$

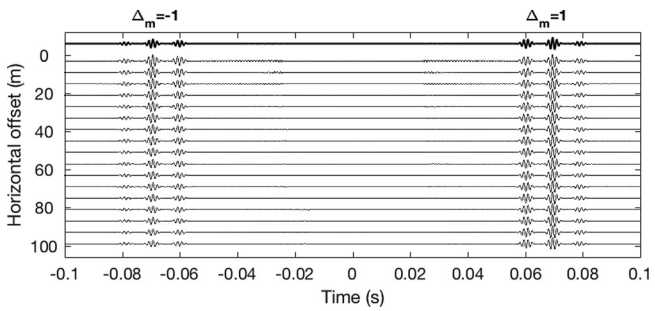

FIG. 6. Waterfall plot of Fig. 5(a) after time delaying according to the seabed sound speed. The direct wave is suppressed, and only every ninth trace is shown. The top trace shows the mean trace for all 200 traces.

The first type of wave *dd* and the fourth type *uu* are symmetrical in time, as are the second type *du* and the third type *ud*. This leads to just two distinct arrival times. The correlation, $c_{j1}^{A}(\tau)$, where $j=1,\ldots,N_R$, is obtained from Eq. (6), with H_j and H_1 replaced by V_j and V_1 and the envelope is shown in Fig. 9(a). Head wave arrivals corresponding to $\Delta_m = 0$, as well as $\Delta_m = \pm 1$ can be seen in Fig. 9(a). In contrast to the HA case shown in Fig. 5(a), even though sources are similarly positioned only on one side of the array, the head waves have both positive and negative slopes [as shown in Fig. 9(a)] due to the receivers being in a vertical array. The dashed and dash-dotted lines predict the arrival times of the head waves. The positive slope head waves in Fig. 9(a) are summed and transformed to the τ–v domain according to

$$Y_V(\tau, v) = \sum_{j=1}^{N_R} h_j c_{j1}^{A}(\tau + (z_j - z_1)\sqrt{v_1^{-2} - v^{-2}}). \tag{10}$$

Figure 9(b) shows the τ-v spectrum (envelope of Y_V on a dB scale) for receivers V_1 to V_{200}. The peaks at -0.07, 0, and $+0.07$ s are due to summing the positive slope head waves for $\Delta_m = 0$, $\Delta_m = \pm 1$ and the resulting peak is at the correct seabed sound speed v_2 (1600 m/s). As with the horizontal array, the procedure to produce the τ-v plot of Fig. 9(b) is equivalent to delay and sum beamforming with time delays based on seabed sound speed rather than steering direction. Figure 9(c) sums over the same time interval as in Fig. 5(c) and obtains the correct seabed sound speed. The peaks in Figs. 9(b) and 9(c) are

narrower in sound speed than for the horizontal array. This is due to the different rate of slope change with seabed sound speed between the horizontal and vertical arrays. For a horizontal array, the rate of slope change with seabed sound speed is constant, $[\partial^2(x_j - x_1)]/[\partial(\delta t)\partial v_2] = 1$, while it is always negative for a vertical array, $[\partial^2(z_j - z_1)]/[\partial(\delta t)\partial v_2] = -[(v_2/v_1)^2 - 1]^{-3/2}$.

B. Vertical array passive (VP)

In this section a vertical array is considered with the sources being random surface wave noise. The time-domain correlation is $c_{j1}^{\mathrm{P}}(\tau)$, with $j = 1,\ldots, N_R$, and is obtained from Eq. (8) for V_j and V_1 and the envelope is shown in Fig. 10(a). Comparing this to case VA in Fig. 9(a), similar V-shaped head waves are observed. However, all the head waves between time lags of -0.2 to $+0.2$ s are observable, instead of just $\Delta_m = 0$ and $\Delta_m = \pm 1$ as in Fig. 9(a). The reason is that the head waves have contributions from noise located over the entire surface, while the active VA has only sources on the left side beyond the critical offset (distance where the incident ray is at the critical angle). Additionally, because of the overhead sources for the VP geometry, it is possible to retrieve direct and reflected waves between receivers as used in the passive fathometer.[15] The direct, surface reflected, and bottom reflected waves are all symmetrical in the time domain. Figure 10(b) shows the τ–v spectrum obtained by delay and summing the positive slope head waves in Fig. 10(a) using Eq. (10) with c_{j1}^{P}. All peaks occur at the seabed sound speed of 1600 m/s. Figure 10(c) sums the response shown in 10(b) over the same interval as for Fig. 5(c).

IV. THE CROSS-BEAM PASSIVE FATHOMETER

In Secs. II and III, a single receiver was chosen to be the virtual source (H_1 for the horizontal array and V_1 for the vertical array). The correlations were computed using the single virtual source on the array and then delayed and summed to produce the τ–v plots. However, there is nothing special about the receiver chosen to be the virtual source. Other receivers could as well have been chosen. To accomplish this, the processing is formulated as a beamformer. This will correlate all combinations of receivers and sum results. Further, this processing allows for optimal gain by using adaptive methods such as the minimum variance distortionless response (MVDR) which will be described later in this section.

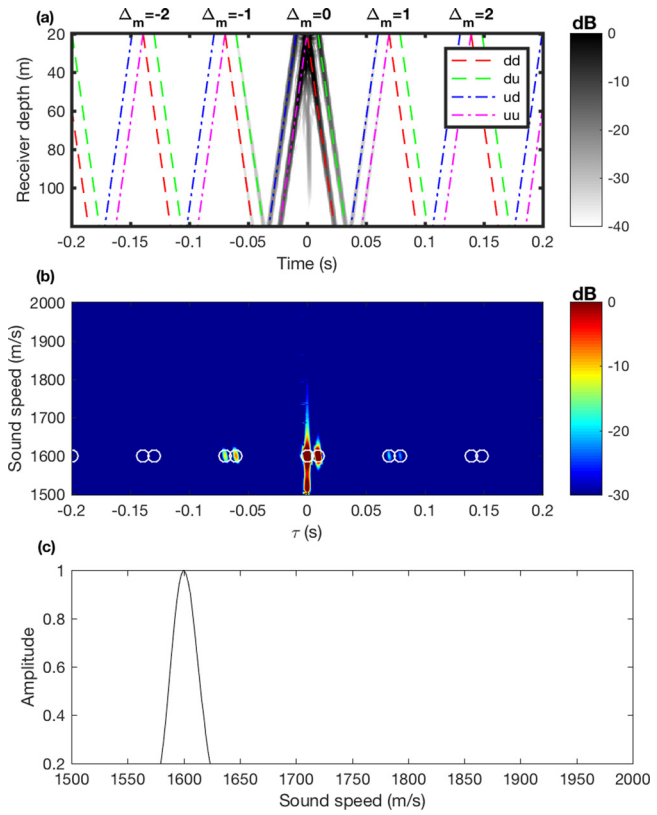

FIG. 9. (Color online) Similar as Fig. 5, but for geometry VA. In panel (a), the envelope of $c_{j1}^{\mathrm{A}}(\tau)$ is shown. In (b), the τ-v spectrum is shown and in (c) the sum of results in panel (b).

The original passive fathometer uses measured noise data from a vertical array and beamforming. But, the processing only uses two beams—a vertically straight up beam and a straight down beam (i.e., endfire beams). However, beam cross-correlations can be performed on many other combinations of beams. This beamforming framework allows one to draw on many techniques to improve signal-to-noise ratio and beam resolution. Although time-domain processing is possible, here all data averaging and beamforming is done in the frequency domain and then transformed to the time domain.

To beamform the data in the frequency domain, the complex pressure along the hydrophone array is written as a

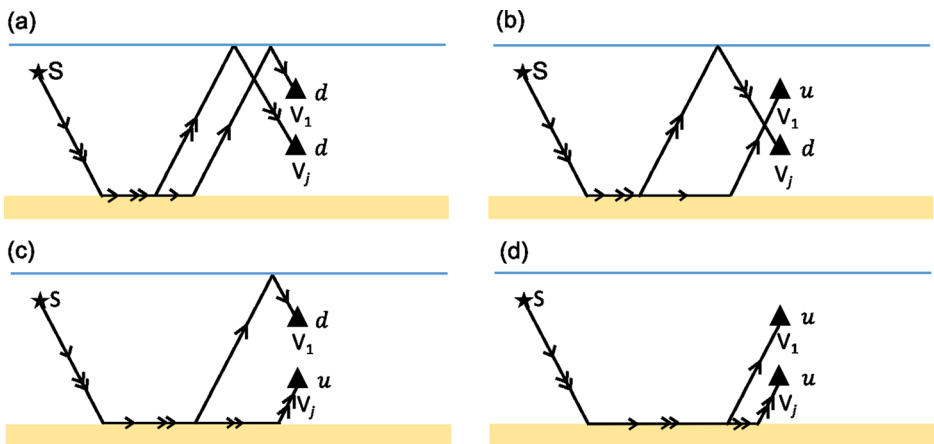

FIG. 8. (Color online) Ray diagram showing paths producing four types of head waves for two vertical array elements, which are labeled as (a) *dd*, (b) *ud*, (c) *du*, and (d) *uu*, respectively. The meaning of labels follows that of Fig. 4.

vector, $\mathbf{p} = [p_1, ..., p_L]^T$ for each of the L hydrophones (suppressing the frequency dependence and T indicates transpose operation). For conventional beamforming, the weight for the lth hydrophone steered at angle θ is

$$w_l = h_l e^{-iz_l\omega(\sin\theta/v_1)} \tag{11}$$

for plane waves arriving at grazing angle θ on hydrophones at depth of z_l and applying a shading window h_l. Writing the steering weights as a vector, $\mathbf{w} = [w_1, \ldots, w_L]^T$, a beam at angle θ is $\mathbf{w}^H\mathbf{p}$, where H represents the Hermitian (conjugate transpose). The conventional beam power for a given direction θ is

$$B(\omega, \theta) = \mathbf{w}^H\mathbf{p}(\mathbf{w}^H\mathbf{p})^H = \mathbf{w}^H\mathbf{p}\mathbf{p}^H\mathbf{w}. \tag{12}$$

The frequency domain form of the correlation function Eq. (8) for a single virtual source is

$$C^{\mathrm{P}}_{j1}(\omega) = p_j(\omega)p_1^*(\omega). \tag{13}$$

This can be extended to include all receivers,

$$C^{\mathrm{P}}_{jk}(\omega) = p_j(\omega)p_k^*(\omega). \tag{14}$$

In matrix form, C^{P}_{jk} forms the entries of the matrix $\mathbf{C}$, referred to as the cross-spectral density matrix (CSDM). For L snapshots of pressure field $\mathbf{p}_l$, $\mathbf{C}$ is estimated from the ensemble average,

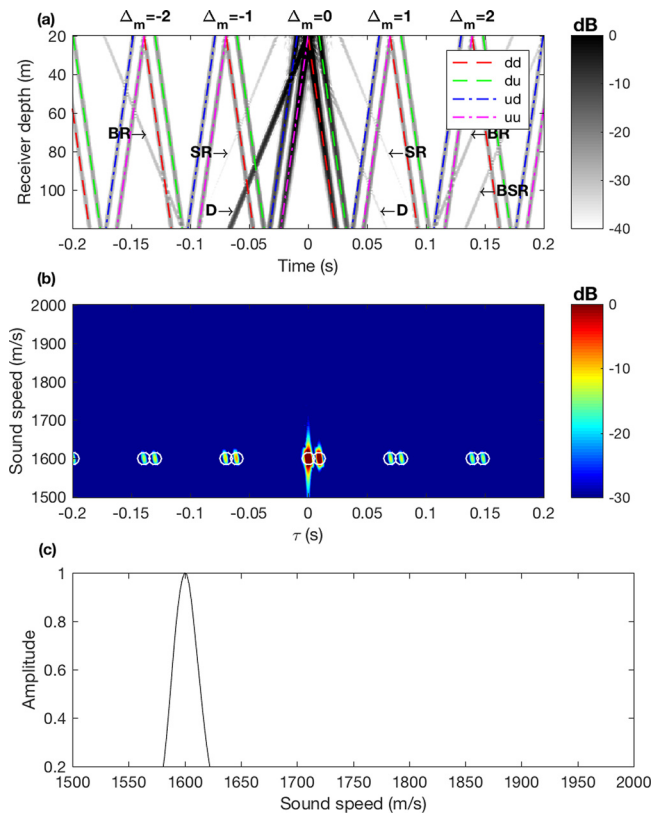

FIG. 10. (Color online) Similar as Fig. 5, but for geometry VP. In panel (a), the envelope of $c^{\mathrm{P}}_{j1}(\tau)$ is shown and other paths such as the direct wave (D), surface-reflected (SR), bottom-reflected (BR) and bottom-surface reflected wave (BSR) are indicated.

$$\mathbf{C} = \sum_{l=1}^{L} \mathbf{p}_l\mathbf{p}_l^H. \tag{15}$$

Forming the CSDM allows for the complex data to be averaged before beamforming. The beam power can be written in terms of the CSDM,

$$B(\omega, \theta) = \mathbf{w}^H\mathbf{C}\mathbf{w}. \tag{16}$$

A. Cross-beam and beam power correlations

The original passive fathometer is a cross-beam correlation between the $+90^\circ$ beam and -90° beam. However, for the cross-beam passive fathometer all positive angles θ are correlated with the corresponding negative angles $-\theta$ (conjugate beams). There is only a slight difference between the beam power output Eq. (16) and the beam cross-correlation at each steering angle (from 0 to 90°) which is[22,23]

$$B_c(\omega, \theta) = \mathbf{w}^H\mathbf{C}\mathbf{w}^*, \tag{17}$$

with subscripts c indicating cross-beam and $*$ is the conjugation operation on $\mathbf{w}$. This is transformed into the time domain,

$$b_c(\tau, \theta) = \mathcal{F}^{-1}[B_c(\omega, \theta)]. \tag{18}$$

The cross-beam processing corresponds to the *du* and *ud* paths in Fig. 8.

In addition to the cross-beam correlation, peaks are visible in the beam power time domain response. This is a correlation of a beam with itself. This is essentially, looking at the *dd* and *uu* paths shown in Fig. 8. In terms of the beam processing, this is simply correlating a beam at angle θ with itself, which is just the beam power Eq. (16). Or, in the time domain,

$$b(\tau, \theta) = \mathcal{F}^{-1}[B(\omega, \theta)]. \tag{19}$$

B. Seismic interferometry versus beamforming

The cross-correlation processing described previously for seismic interferometry can be compared to the beamforming framework. For a single virtual source (in a vertical receiver array) at V_1, the τ–v summing in Eq. (10) can be written in terms of the angle θ instead of velocity by using Snell's law,

$$\theta = \sin^{-1}\sqrt{1 - \left(\frac{v_1}{v}\right)^2}, \tag{20}$$

leading to

$$Y_{\mathrm{V}}(\tau, \theta) = \sum_{j=1}^{N_R} h_j c^{\mathrm{P}}_{j1}\left(\tau + (z_j - z_1)\frac{\sin\theta}{v_1}\right). \tag{21}$$

Correlations are also possible for virtual sources other than at the position of receiver 1. Extending this to include any

receiver $1,\ldots,N_R$ requires the correlations to be taken over all combinations (c^{P}_{jk}), and Y_{V} therefore requires a double sum,

$$Y_{\mathrm{V}}(\tau,\theta)=\sum_{j=1}^{N_R}\sum_{k=1}^{N_R}h_j h_k c^{\mathrm{P}}_{jk}\left(\tau+(z_j-z_k)\frac{\sin\theta}{v_1}\right). \tag{22}$$

This is expressed in the frequency domain by using the time shifting property of the Fourier transform,

$$\begin{aligned}Y_{\mathrm{V}}(\omega,\theta)&=\sum_{j=1}^{N_R}\sum_{k=1}^{N_R}h_j h_k C^{\mathrm{P}}_{jk}(\omega)e^{i(z_j-z_k)\omega(\sin\theta/v_1)}\\&=\sum_{j=1}^{N_R}h_j e^{iz_j\omega(\sin\theta/v_1)}\sum_{k=1}^{N_R}h_k C^{\mathrm{P}}_{jk}(\omega)e^{-iz_k\omega(\sin\theta/v_1)}\\&=\sum_{j=1}^{N_R}w_j^*\sum_{k=1}^{N_R}C^{\mathrm{P}}_{jk}(\omega)w_k=\mathbf{w}^H\mathbf{C}\mathbf{w}\,,\end{aligned} \tag{23}$$

where we have substituted the steering vector Eq. (11). This is equal to the beam power Eq. (16). Since this is a cross-correlation, the time delay can also be applied as a sum z_j+z_k instead of a difference. In that case,

$$\begin{aligned}Y_{\mathrm{V}}(\omega,\theta)&=\sum_{j=1}^{N_R}\sum_{k=1}^{N_R}h_j h_k C^{\mathrm{P}}_{jk}(\omega)e^{i(z_j+z_k)\omega(\sin\theta/v_1)}\\&=\sum_{j=1}^{N_R}h_j e^{iz_j\omega(\sin\theta/v_1)}\sum_{k=1}^{N_R}h_k C^{\mathrm{P}}_{jk}(\omega)e^{iz_k\omega(\sin\theta/v_1)}\\&=\sum_{j=1}^{N_R}w_j^*\sum_{k=1}^{N_R}C^{\mathrm{P}}_{jk}(\omega)w_k^*=\mathbf{w}^H\mathbf{C}\mathbf{w}^*,\end{aligned} \tag{24}$$

which is equal to the cross-beam correlation $B_c(\omega,\theta)$ in Eq. (17). This expression can be transformed to the time domain, $\mathcal{F}^{-1}[Y_{\mathrm{V}}(\omega,\theta)]$ and is equal to the time domain cross-beam correlation $b_c(\tau,\theta)$ in Eq. (18).

The arrival times for the cross-beam noise correlation is given by Eq. (4). As with Eq. (9), for a vertical array the first terms involving the range of the receivers cancels as does the z_s term since the noise sources are very near the surface and only have down going propagation. Further, for the cross-beams, only the paths with opposite signs are considered and all arrivals are aligned through beamforming as if they are all at z_1. This simplifies Eq. (4) to

$$\delta t=(Z(m-n)-z_1)\frac{2\sin\theta_c}{v_1}. \tag{25}$$

One caveat to this comparison between beamforming and seismic interferometry is important. In beamforming, relative sensor locations are used. That is, a single sensor is taken at the phase reference when constructing steering vectors. This impacts the cross-beam correlations comparisons to interferometry and leads to an offset in $b_c(\tau,\theta)$ that depends on the reference sensor. For example, here the beamforming uses the sensor at z_1 as the phase reference leading to a modified steering vector $\tilde{w}$,

$$\tilde{w}_l=w_l e^{iz_1\omega(\sin\theta/v_1)}=e^{-i(z_l-z_1)\omega(\sin\theta/v_1)}. \tag{26}$$

When processed for the time domain cross-beam correlation $b_c(\tau,\theta)$, the beamforming has a time shift relative to the interferometry of $2z_1(\sin\theta_c/v_1)$.

To illustrate, the acoustic interferometry and beamforming results are compared using the simulations in Sec. III. In Fig. 11, beamforming results and interferometry results are identical with the exception of the interferometry results are centered at lag time zero and this differs from the beamformer by a lag time $2z_1(\sin\theta_c/v_1)\approx 9.3$ ms. Based on seabed sound speed of 1600 m/s, the peaks [Eq. (25)] are shown as the open circles in Fig. 11.

This section showed that seismic interferometry, when considering all receivers as virtual sources, is equivalent to delay and sum beamforming. If the delay introduced is $\pm(z_j+z_k)$, the result is equivalent to cross-beam processing. If the delay is $\pm(z_j-z_k)$, the result is equivalent to the beam power correlation. The significance of this is that once cast as a beamforming operation, adaptive methods can be applied to enhance the results and this will be described next in Sec. IV C.

C. Adaptive beamforming

With the seismic interferometry processing cast as a beamforming operation, one can exploit many of the beamforming techniques for improving performance, for example using adaptive beamforming. As for the original passive fathometer, adaptive beamforming often provides improved cross-correlation estimates.[22] Here, MVDR is used[37,38] for the data analyzed. To adaptively beamform using MVDR, the steering weights $\tilde{\mathbf{w}}$ are computed according to

$$\tilde{\mathbf{w}}=\frac{\mathbf{C}^{-1}\mathbf{w}}{\mathbf{w}^H\mathbf{C}^{-1}\mathbf{w}}, \tag{27}$$

where $\mathbf{w}$ is the previously defined delay and sum weight. The adaptive weight $\tilde{\mathbf{w}}$ is used in Eq. (17), but for adaptive processing, the weights for beams at $+\theta$ are not necessarily equal to the conjugate of beams at $-\theta$ as for conventional processing [i.e., $\tilde{\mathbf{w}}(\theta)\neq\tilde{\mathbf{w}}^*(-\theta)$]. Therefore the expression for the adaptive beam power and cross-beam correlation are

$$\tilde{B}(\omega,\theta)=\tilde{\mathbf{w}}(\theta)^H\mathbf{C}\tilde{\mathbf{w}}(\theta), \tag{28}$$

$$\tilde{B}_c(\omega,\theta)=\tilde{\mathbf{w}}(\theta)^H\mathbf{C}\tilde{\mathbf{w}}(-\theta). \tag{29}$$

As before, the time-series is the inverse Fourier transform of $\tilde{B}_c(\omega,\theta)$ or $\tilde{B}(\omega,\theta)$.

V. EXPERIMENTAL RESULTS

Results from several experiments demonstrate the head wave detection performance of the cross-beam with adaptive processing. In these experiments, the arrays are much shorter and use fewer hydrophones than in the previous simulations. The experimental arrays vary in length from 3 to 16 m. However, correlation peaks can be seen and used to determine seabed sound speed. Four

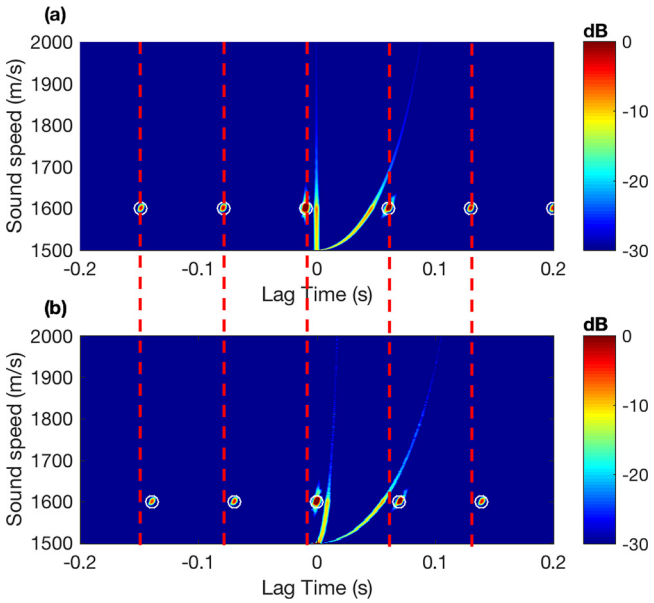

FIG. 11. (Color online) Comparison of cross-beam correlation (a) and interferometric processing (b) for 100 m vertical array with seabed sound speed of 1600 m/s and water depth of 150 m (see Fig. 2). Circles indicate the expected locations. The two panels are identical with the exception that the interferometric processing centers the correlations around time zero. The difference in time lag is $2z_1(\sin\theta_c/v_1) \approx 9.3$ ms in this case.

experiments will be described and each of these were in different locations and times using equipment that varied (e.g., array lengths, hydrophone spacing). The experiments were conducted by the NATO centre for maritime research and experimentation (CMRE). The cross beam processing was used in all cases with adaptive processing Eq. (29). The beam correlation results as a function of angle (θ) were converted to a sound speed dependence using Snell's law.

A. GLISTEN'15 experiment

The GLISTEN'15 experiment is the most recent of the data sets (September 6, 2015) and was conducted off the coast of the island of Capraia, Italy. Noise data were collected on a moored array in about 100 m water depth at the location 43°6.678′N, 10°20.028′E. The array had 32 hydrophones with 0.15 m spacing. Some of the hydrophones were not operating correctly and so a sub-set of 22 hydrophones (contiguous at 0.15 m spacing) was used for this analysis. The data were sampled at 50 kHz and Fourier transformed using 16 384 point snapshots for the CSDM, **C**, averaging after taking the fast Fourier transform (FFT). At this spacing, the cut-off frequency for beamforming is 5000 Hz. Using the entire 5000 Hz band led to many artifacts in the passive fathometer output. However, by limiting to a 500 Hz band (1500–2000 Hz) the results showed a reasonable set of arrivals in approximately the expected location based on water depth and array depth. For this data period, the wind speed was measured to be around 15 kn and a 5 min average of data was processed to make the figure. Results are shown in Fig. 12(a) along with calculated expected lag times. The exact seabed sound speed at this location is not known but can be compared to results from an analysis that was done at a nearby location and at the same plateau using a time-frequency geo-acoustic inversion and a controlled source. They found an average sound speed in the top 6 m of 1530 m/s (Ref. 39, Table III) which is close to the 1525 m/s found here.

B. ASCOT'01 experiment

The ASCOT'01 experiment took place off the United States east coast. The array was moored in about 100 m of water at the location 42°40.163′N, 70°10.614′W and had 64 hydrophones of which 32 at 0.5 m spacing were used for this analysis allowing beamforming up to 1500 Hz. The data were sampled at 6 kHz and Fourier transformed using 2048 point snapshots for CSDM averaging after taking the FFT. For this experiment, the focus was on recording a variety of broadband transmissions and was therefore not ideal for noise experiments. However, on June 15, 2001 the transmissions were limited in duration and frequency so the array data could be used for noise in the 50−800 Hz band (the actual band used for analysis was a 500 Hz band from 200−700 Hz). Total averaging time for the data was 6 min. The wind speed was not recorded but the sea-state was recorded as 2−3 which is sufficient for producing surface wave noise. The results are not very conclusive, but the purpose for including them here is to show that in some cases less defined peaks occur. The likely location of peaks was consistent with a higher seabed sound speed. Results are shown in Fig. 12(b) with a more broken pattern in the correlations compared to the other experiments. The cause for this is unclear at this point but may be due to seabed layering or scattering or simply insufficient wind noise. No comparison data for seabed sound speed were available for this site.

C. Boundary'03 experiment

The Boundary'03 experimental data set is the same one that was used in the original passive fathometer development.[15,22] The experiment was conducted off the coast of Sicily, Italy. A free drifting array was used and had 32 hydrophones spaced at 0.18 m for a maximum frequency of 4.2 kHz and a sampling frequency of 12 kHz. The array was mostly isolated from other sources of sound so measurements were essentially noise due to wind and waves. The data were sampled at 12 kHz and Fourier transformed using 4096 point snapshots for the FFT. Total averaging time was 3.5 min. The wind varied during the experiment but was, on average, approximately 15 kn. The exact array position was not recorded while drifting but the array depth was designed to keep the hydrophones between 70 and 80 m and the water depth was approximately 130 m. In Fig. 1, the cross-beam processing was applied over the entire band of 50−4000 Hz using Eq. (29), however, in that figure the y-axis is in angle space rather than being converted to sound speed. In Fig. 12(c) results are shown with the band limited to 500 Hz (3500−4000 Hz) and is in terms of sound speed rather than angle. Limiting the bandwidth improved the localization of the peaks (comparing Figs. 1 and 12). Since the array was drifting in this experiment there were no complementary

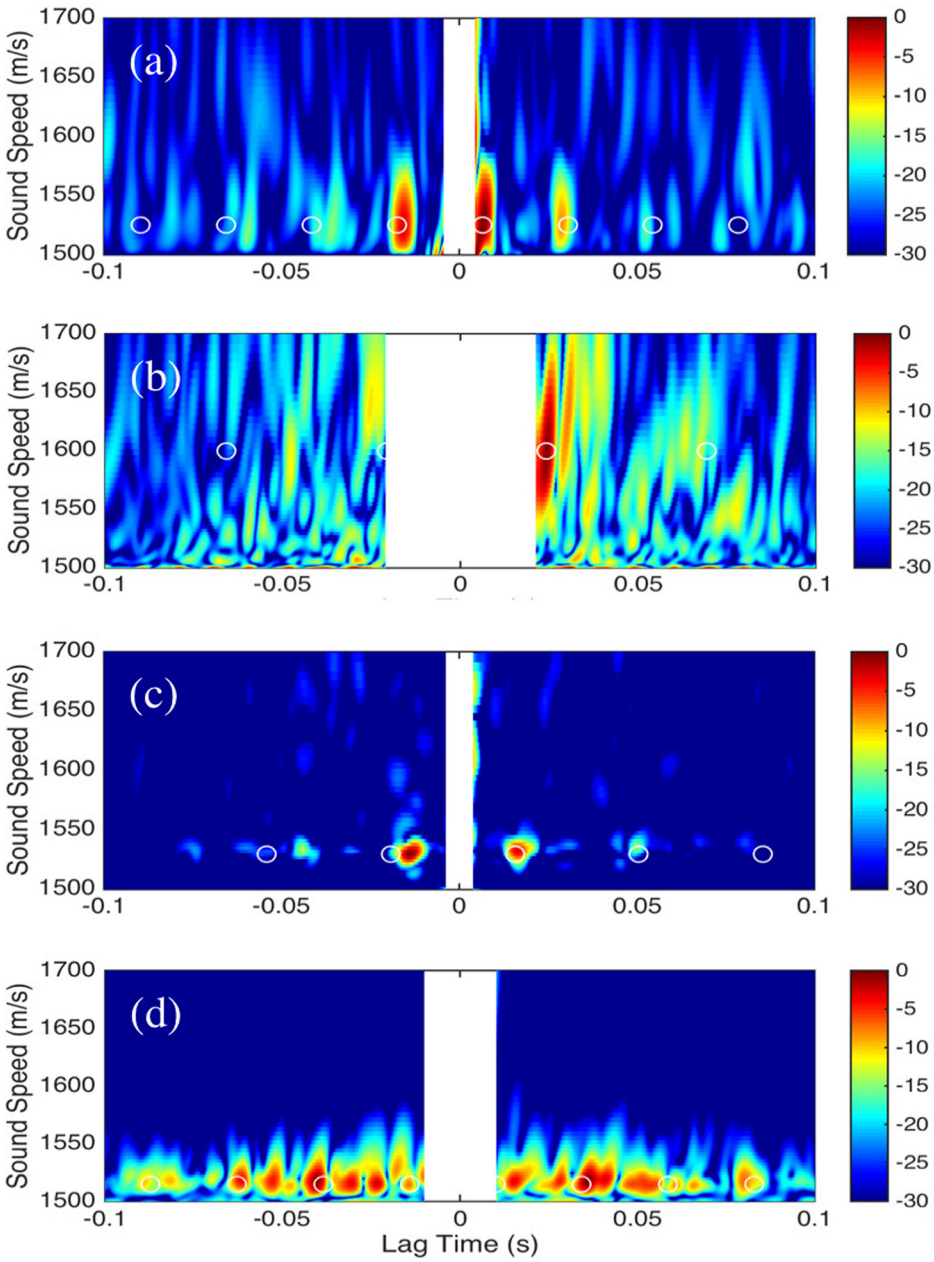

FIG. 12. (Color online) Cross-beam correlation using experimentally measured ambient noise data for four sites with different conditions and equipment. (a) GLISTEN'15, (b) ASCOT'01, (c) Boundary'03, and (d) MAPEX2000 data.

experiments to verify seabed properties at the exact location. However, the results are on the Malta Plateau where many locations have been surveyed and had geo-acoustic inversions performed[40,41] and the seabed sound speed estimated here is consistent with those.

D. MAPEX2000 experiment

The MAPEX2000 experiments were conducted near the island of Sicily, Italy. These data were collected relatively near the drifting array measurements described above for the Boundary'03 data. For the MAPEX2000 experiment, the array was moored in about 130 m water depth at the location, 36°26.673′N, 14°46.535′E and these data were taken on Nov. 22, 2000. The array had 64 hydrophones of which 32 of them spaced at 0.5 m (i.e., 1500 Hz array design frequency) were used for this analysis. The data were sampled at 6 kHz and Fourier transformed using 2048 point snapshots for averaging after taking the FFT. Total averaging time was 7.5 min. The 500 Hz band from 200–700 Hz is used here. The wind speed, as measured on the research vessel anemometer (located near the array) was 15–20 knots during the experimental time. Results are shown in Fig. 12(d). For comparison, the site where this data was collected is near the site where geo-acoustic inversions were performed using a controlled source[42] where the seabed sound speed was found to be 1554 m/s in the top 18.9 m.

The seabed sound speed can also be estimated for each of these datasets by summing the cross-beam responses (shown in Fig. 12) over lag time as was done for the simulation data. The maxima should occur at locations of seabed sound speed. Figure 13 shows the seabed sound speed maxima for each of the previous experiments described. In all

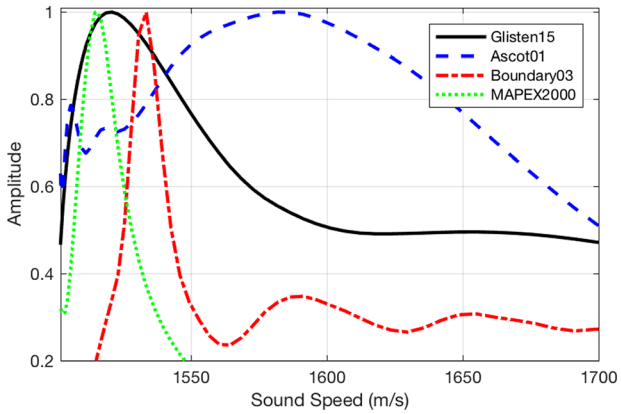

FIG. 13. (Color online) Sum over time lag of cross-beam response showing seabed sound speed maxima. GLISTEN'15 (solid), ASCOT'01 (dashed), Boundary'03 (dash-dot), and MAPEX2000 (dotted) data.

cases, a peak is evident which indicates the likely value for the seabed sound speed.

To illustrate, the beam power correlations for the simulation described previously in Sec. IV is considered again here using beam power rather than cross-beams. In panel (a) of Fig. 14 the beam power correlation is shown for the simulation and in panel (b), the beam power correlation for the Boundary'03 experiment is shown for the same conditions and processing parameters as previously described for the cross-beams. Although the beam power correlations are perfectly symmetric in time lag, both the positive and negative times are shown for easier comparison with the results from the cross-beams. The Boundary'03 result was the only one of the four previously presented experimental data sets that showed clear beam power correlation peaks. The other sites were not nearly as clean and the reason for this is unclear at this point.

VI. DISCUSSION AND CONCLUSION

Using simulations, the head wave was shown here to be detectable not only on horizontal arrays but also with vertical arrays using either ocean noise or controlled, active sources. The experimental data confirm the detection of these head waves in ocean ambient noise. The Boundary'03 data provided the best example. In that case, the cross-beams showed clearly localized arrivals in time and sound speed very similar to what was shown in the simulations. The water depth, array depth and water column sound speed were inserted into Eq. (25) and the sound speed in the sediment was adjusted to 1530 m/s to predict cross-beam correlation arrivals. These were included as circles in Fig. 12 and align with the measured peaks reasonably well. Note that the actual water column sound speed is not uniform so slight refraction could cause some error in predicted versus measured positions. The Boundary'03 data also showed predictable peaks for the beam power correlations.

The other three data sets were of varying quality. The GLISTEN'15 data had some hydrophone issues which may have contributed to lower quality of the cross-beam estimates. The ASCOT'01 data showed the poorest peak locations but this experiment was not designed to measure noise. The array gain was likely not optimized for noise measurements and there were nearby research vessels as well as active transmissions. The data had to be sliced out of various files to construct a noise average. The wind speed was not extremely high so the overall quality of this experimental data for this analysis is far from ideal. The MAPEX2000 data were of reasonable quality and show a significant amount of energy in the cross-correlation at around 1517 m/s. The peaks are not as well localized in time as for the simulations or Boundary'03 data. This may be due to a variety of factors that are not well understood (e.g., layering in the seabed or scattering).

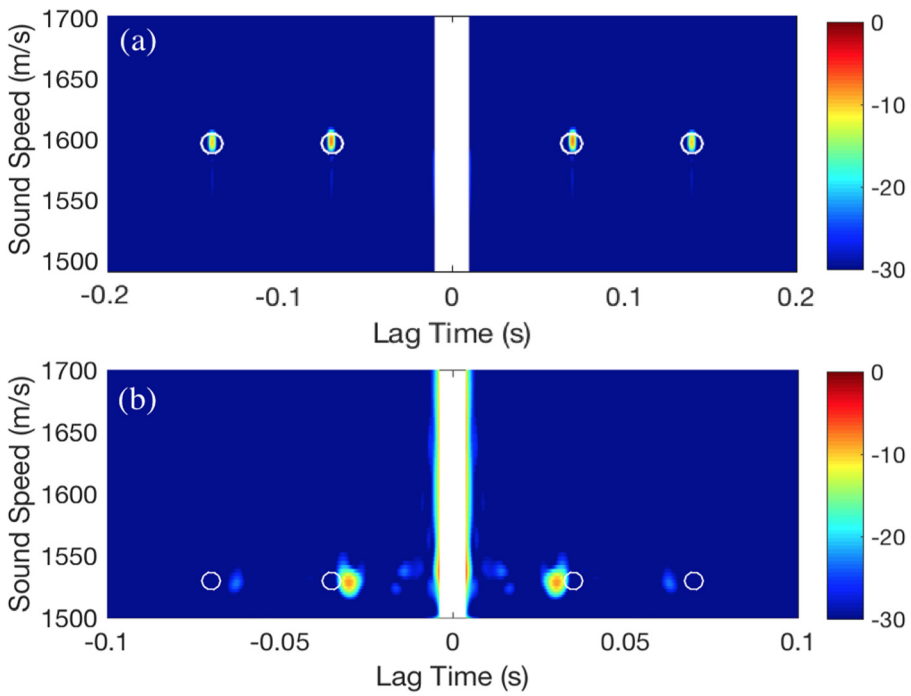

FIG. 14. (Color online) In panel (a) a simulation of beam power correlation is shown for the geometry described in Sec. IV. In (b), experimental data are shown for the beam power correlation from the Boundary'03 experiment. Note, the time axes are not the same in the two panels.

The head wave has here been explored using both horizontal and vertical arrays and previous work was expanded on to include not only active sources but also ambient noise such as that generated in the ocean from surface waves. Both modeling and experimental data show that this head wave can be passively observed in the ocean using ambient noise on vertical hydrophone arrays. The seismic interferometric processing described is identical to delay-and-sum, cross-correlating beams when all receivers are combined as virtual sources. The cross-beam correlation processing was further optimized using adaptive beamforming. Although the beamforming framework is equivalent to the interferometry processing in the seismic literature, the beamforming approach can provide processing gain especially for the adaptive methods.

ACKNOWLEDGMENTS

The authors would like to gratefully acknowledge support for this research by the Office of Naval Research Ocean Acoustics Program under Grant No. N00014-13-1-0632. We also would like to acknowledge the NATO Centre for Maritime Research and Experimentation as well as Peter Nielsen, Chris Harrison, and Jurgen Sellschopp for their collaborations and help in providing the experimental data.

[1]G. T. Schuster, *Seismic Interferometry* (Cambridge University Press, Cambridge, UK, 2009).
[2]L. A. Brooks and P. Gerstoft, "Green's function approximation from cross-correlation of active sources in the ocean," J. Acoust. Soc. Am. **126**(1), 46–55 (2009).
[3]K. Wapenaar, D. Draganov, R. Snieder, X. Campman, and A. Verdel, "Tutorial on seismic interferometry: Part 1: Basic principles and applications," Geophys. **75**(5), A195–A209 (2010).
[4]P. Roux, W. A. Kuperman, and NPAL Group, "Extracting coherent wave fronts from acoustic ambient noise in the ocean," J. Acoust. Soc. Am. **116**(4), 1995–2003 (2004).
[5]P. Roux, K. G. Sabra, W. A. Kuperman, and A. Roux, "Ambient noise cross correlation in free space: Theoretical approach," J. Acoust. Soc. Am. **117**(1), 79–84 (2005).
[6]K. G. Sabra, P. Roux, and P. W. A. Kuperman, "Emergence rate of the time-domain Green's function from the ambient noise cross-correlation function," J. Acoust. Soc. Am. **118**(6), 3524–3531 (2005).
[7]R. Snieder, K. Wapenaar, and K. Larner, "Spurious multiples in seismic interferometry of primaries," Geophys. **71**(4), SI111–SI124 (2006).
[8]D. Mikesell, K. van Wijk, A. Calvert, and M. Haney, "The virtual refraction: Useful spurious energy in seismic interferometry," Geophys. **74**(3), A13–A17 (2009).
[9]S. King and A. Curtis, "Suppressing nonphysical reflections in Green's function estimates using source−receiver interferometry," Geophys. **77**(1), Q15–Q25 (2012).
[10]O. A. Godin, N. R. Chapman, M. C. A. Laidlaw, and D. E. Hannay, "Head wave data inversion for geoacoustic parameters of the ocean bottom off Vancouver Island," J. Acoust. Soc. Am. **106**(5), 2540–2551 (1999).
[11]J. W. Choi and P. H. Dahl, "First-order and zeroth-order head waves, their sequence, and implications for geoacoustic inversion," J. Acoust. Soc. Am. **119**(6), 3660–3668 (2006).
[12]C. H. Harrison and M. Siderius, "Using beam-beam cross-correlation of noise to investigate back-scatter," in *Proceedings of the Eighth European Conference on Underwater Acoustics, 8th ECUA 2006*.
[13]J. Gebbie and M. Siderius, "Head wave correlations in ambient noise," J. Acoust. Soc. Am. **140**(1), EL62–EL66 (2016).
[14]C. H. Harrison and D. G. Simons, "Geoacoustic inversion of ambient noise: A simple method," J. Acoust. Soc. Am. **112**(4), 1377–1389 (2002).
[15]M. Siderius, C. H. Harrison, and M. B. Porter, "A passive fathometer technique for imaging seabed layering using ambient noise," J. Acoust. Soc. Am. **120**(3), 1315–1323 (2006).
[16]L. Muzi, M. Siderius, J. E. Quijano, and S. E. Dosso, "High-resolution bottom-loss estimation using the ambient-noise vertical coherence function," J. Acoust. Soc. Am. **137**(1), 481–491 (2015).
[17]J. E. Quijano, S. E. Dosso, J. Dettmer, L. M. Zurk, M. Siderius, and C. H. Harrison, "Bayesian geoacoustic inversion using wind-driven ambient noise," J. Acoust. Soc. Am. **131**(4), 2658–2667 (2012).
[18]K. G. Sabra, P. Roux, A. M. Thode, G. L. D'Spain, W. S. Hodgkiss, and W. A. Kuperman, "Using ocean ambient noise for array self-localization and self-synchronization," IEEE J. Ocean. Eng. **30**(2), 338–347 (2005).
[19]L. A. Brooks and P. Gerstoft, "Green's function approximation from cross-correlations of 20−100 Hz noise during a tropical storm," J. Acoust. Soc. Am. **125**(2), 723–734 (2009).
[20]O. A. Godin, M. G. Brown, N. A. Zabotin, L. Y. Zabotina, and N. J. Williams, "Passive acoustic measurement of flow velocity in the Straits of Florida," Geosci. Lett. **1**(1), 16 (2014).
[21]C. H. Harrison and M. Siderius, "Bottom profiling by correlating beam-steered noise sequences," J. Acoust. Soc. Am. **123**(3), 1282–1296 (2008).
[22]M. Siderius, H. C. Song, P. Gerstoft, W. S. Hodgkiss, P. Hursky, and C. H. Harrison, "Adaptive passive fathometer processing," J. Acoust. Soc. Am. **127**(4), 2193–2200 (2010).
[23]P. Gerstoft, W. S. Hodgkiss, M. Siderius, C. F. Huang, and C. H. Harrison, "Passive fathometer processing," J. Acoust. Soc. Am. **123**(3), 1297–1305 (2008).
[24]J. Traer, P. Gerstoft, and W. S. Hodgkiss, "Ocean bottom profiling with ambient noise: A model for the passive fathometer," J. Acoust. Soc. Am. **129**(4), 1825–1836 (2011).
[25]J. Traer and P. Gerstoft, "Coherent averaging of the passive fathometer response using short correlation time," J. Acoust. Soc. Am. **130**, 3633–3641 (2011).
[26]F. B. Jensen, W. A. Kuperman, M. B. Porter, and H. Schmidt, *Computational Ocean Acoustics* (Springer Science & Business Media, New York, 2011).
[27]D. A. Bevans and M. J. Buckingham, "Estimating the sound speed of a shallow-water marine sediment from the head wave excited by a low-flying helicopter," J. Acoust. Soc. Am. **142**(4), 2273–2287 (2017).
[28]S. King and A. Curtis, "Velocity analysis using both reflections and refractions in seismic interferometry," Geophys. **76**(5), SA83–SA96 (2011).
[29]K. Wapenaar and J. Fokkema, "Green's function representations for seismic interferometry," Geophys. **71**(4), SI33–SI46 (2006).
[30]J. Li, P. Gerstoft, D. Z. Gao, G. F. Li, and N. Wang, "Localizing scatterers from surf noise cross correlations," J. Acoust. Soc. Am. **141**(1), EL64–EL69 (2017).
[31]L. A. Brooks and P. Gerstoft, "Ocean acoustic interferometry," J. Acoust. Soc. Am. **121**(6), 3377–3385 (2007).
[32]A. Kaslilar, U. Harmankaya, K. Wapenaar, and D. Draganov, "Estimating the location of a tunnel using correlation and inversion of Rayleigh wave scattering," Geophys. Res. Lett. **40**, 6084–6088, https://doi.org/10.1002/2013GL058462 (2013).
[33]G. A. Meles and A. Curtis, "Physical and non-physical energy in scattered wave source−receiver interferometry," J. Acoust. Soc. Am. **133**(6), 3790–3801 (2013).
[34]H. Schmidt and F. B. Jensen, "A full wave solution for propagation in multilayered viscoelastic media with application to Gaussian beam reflection at fluid–solid interfaces," J. Acoust. Soc. Am. **77**(3), 813–825 (1985).
[35]H. Schmidt, Oases 3.1 User Guide and Reference Manual, Massachusetts Institute of Technology Cambridge, MA, http://acoustics.mit.edu/faculty/henrik/oases.html, 2004.
[36]W. A. Kuperman and F. Ingenito, "Spatial correlation of surface generated noise in a stratified ocean," J. Acoust. Soc. Am. **67**(6), 1988–1996 (1980).
[37]H. L. Van Trees, *Detection, Estimation, and Modulation Theory, Optimum Array Processing* (Wiley, New York, 2004).
[38]W. S. Burdic, *Underwater Acoustic System Analysis* (Prentice-Hall, Englewood Cliffs, NJ, 1991).
[39]C. Holland and J. Osler, "High-resolution geoacoustic inversion in shallow water: A joint time-and frequency-domain technique," J. Acoust. Soc. Am. **107**(3), 1263–1279 (2000).
[40]C. Holland, R. Hollett, and L. Troiano, "Measurement technique for bottom scattering in shallow water," J. Acoust. Soc. Am. **108**(3), 997–1011 (2000).
[41]C. Holland, R. Gauss, P. Hines, P. Nielsen, J. Preston, C. Harrison, D. Ellis, K. LePage, J. Osler, and R. Nero, "Boundary characterization experiment series overview," IEEE J. Ocean. Eng. **30**(4), 784–806 (2005).
[42]M. Siderius, P. Nielsen, and P. Gerstoft, "Range-dependent seabed characterization by inversion of acoustic data from a towed receiver array," J. Acoust. Soc. Am. **112**(4), 1523–1535 (2002).